Experiments in Fluids 15, 133–146 (1993)

Experiments in Fluids

Particle tracking velocimetry in three-dimensional flows

Part 1. Photogrammetric determination of particle coordinates

H. G. Maas, A. Gruen, D. Papantoniou

Swiss Federal Institute of Technology, ETH-Hoenggerberg, CH-8093 Zürich, Switzerland

Received: 17 June 1992 / Accepted: 20 January 1993

Abstract. Particle Tracking Velocimetry (PTV) is a well-known technique for the determination of velocity vectors within an observation volume. However, for a long time it has rarely been applied because of the intensive effort necessary to measure coordinates of a large number of flow marker particles in many images. With today's imaging hardware in combination with the methods of digital image processing and digital photogrammetry, however, new possibilities have arisen for the design of completely automatic PTV systems. A powerful 3*D* PTV has been developed in a cooperation of the Institute of Geodesy and Photogrammetry with the Institute of Hydromechanics and Water Resources Management at the Swiss Federal Institute of Technology. In this paper hardware components for 3*D* PTV systems wil be discussed, and a strict mathematical model of photogrammetric 3*D* coordinate determination, taking into account the different refractive indices in the optical path, will be presented. The system described is capable of determining coordinate sets of some 1000 particles in a flow field at a time resolution of 25 datasets per second and almost arbitrary sequence length completely automatically after an initialization by an operator. The strict mathematical modelling of the measurement geometry, together with a thorough calibration of the system provide for a coordinate accuracy of typically 0.06 mm in X, Y and 0.18 mm in Z (depth coordinate) in a volume of $200 \times 160 \times 50$ mm^3.

1 Introduction

3D PTV is based on discrete visualization of flows with small, reflecting, neutrally buoyant tracer particles and a stereoscopic recording of image sequences of the particles marking the flow with the aim of determining 3D coordinates of the tracers to derive their trajectories. Compared with competing flow measurement techniques, PTV shows some interesting advantages, as shown in Table 1.

While Hotwire Anemometry and Laser Doppler Anemometry (LDA) allow for large temporal resolutions of a velocity measurement at a point, and Particle Imaging Velocimetry (PIV, Adrian 1986) yields a very high spatial resolution of velocity vectors in a 2D observation sheet, 3D PTV is a technique which allows the determination of a large number of long 3D trajectories of discrete particles in a fully 3D observation volume. The temporal resolution, however, is limited to the imaging rates of solid state sensor cameras. Unlike other methods, PTV is based on the coordinate measurement and tracking of individual particles, which requires a reliable identification, multi-image matching, coordinate determination and multi-temporal matching of each individual particle. With large numbers of particles in the flow this process leads to ambiguities which cannot always be resolved, so that the spatial resolution of PTV will always be somewhat limited. Therefore, the main effort in the development of algorithms for a high resolution 3D PTV must be focused on careful handling of these ambiguities, which necessitates strict geometric modelling of the multimedia environment, the use of at least three synchronous cameras imaging the flow and a thorough calibration of the system. Fig. 1 shows a flow chart of such a system, whose components will be described in this article, except the tracking in object space and the 3D interpolation, which will be addressed in Part II of this publication (Malik et al., 1993):

Table 1. Comparison of performance features of some flow measurement techniques

	Hotwire	LDA	PIV	PTV
Spatial resolution	low	low	very high	high
temporal resolution	high	very high	very low	low
velocity range	high	very high	very high	low
dimensions of observation volume	–	–	2	2–3
dimensions of velocity field	1–3	1–3	2	2–3
result	vectors	vectors	vectors	trajectories

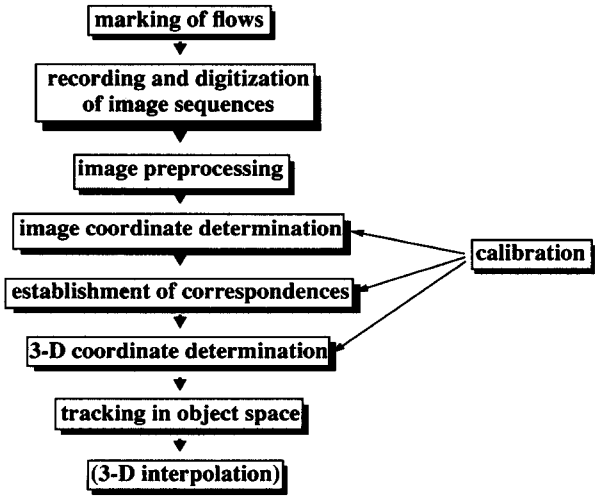

Fig. 1. Flow scheme of 3D PTV

2 Previous work

Though PTV is one of the oldest techniques of flow measurement, the acquisition of quantitative information of high density at reasonable effort has only become possible in the last two decades. The methods and applications reported in the literature show a transition from systems with completely manual data processing (i.e. a human operator measures coordinates and defines correspondences) towards completely automated systems. Besides the degree of automation, the reported methods differ in the spatial and temporal information density achieved and the quality of the geometric modelling. Many of the methods are restricted to two-dimensional velocity measurements, while three-dimensional approaches often observe trajectories of only a few particles. Early applications use movie cameras or photos and pulsed illumination and the images are measured manually. Later users turned to digitization of film and automatic or semi-automatic image processing. Recent applications often use solid state sensor cameras, which allow online data processing.

An early application based on stereoscopic imaging is reported by Chiu and Rib (1956); their method requires manual measurements in the images. Jacobi (1980) reports a first application with strict photogrammetric modelling of the multimedia geometry; the evaluation is also performed manually, but Jacobi is working with only one particle at a time. Many systems use a Bolex stereo lens with two parallel optics arranged on a base which corresponds to the human eye disparity of about 65 mm imaging onto the left and right half of one film. Due to the parallel optical axis this lens can save some calibration effort, but the short baselength leads to very inhomogeneous accuracies of the three coordinates: the error in the depth coordinate will usually be an order of magnitude larger than the error in the plane coordinates. Sheu et al. (1982) used this kind of lens to image particles in a volume of $200 \times 160 \times 15$ mm^3; the manual measurement of 70 trajectories takes about 20 hours. Chang et al. (1985a, b) used similar equipment, but they digitize the film onto 2048×2048 pixels and apply simple image processing methods to derive the particle image coordinates. They achieve 92 trajectories with an estimated accuracy of 25 μm/25 μm/1046 μm in the X, Y, Z components. A system based on electronic imaging is presented by Adamczyk and Rimai (1988); they strictly limit the number of particles to avoid problems with unresolvable ambiguities and determine up to 16 trajectories. Koyabashi et al. (1989) use two CCD cameras to measure a flow between rotating disks and achieve an average of 51 simultaneous velocity vectors. An advanced development has been presented by a group at Tokyo University (Nishino and Kasagi 1989, Sata et al. 1989, Nishino et al. 1989, Kasagi and Nishino 1990). Nishino et al. have developed a completely automatic 3D PTV, which allows the determination of up to 440 simultaneous velocity vectors.

The development of the 3D PTV system described here started in 1987 (Papantoniou and Dracos, 1990a, b; Papantoniou and Maas, 1990; Maas, 1990). It is based on methods of digital photogrammetry and recording particle image sequences by three synchronized CCD cameras. It has been applied to the measurements of velocity fields in test volumes of $120 \times 120 \times 15$ to $200 \times 200 \times 40$ mm^3 seeded with about 1000–1500 particles in a 24 m laboratory channel and in a stirred aquarium.

3 Hardware

The hardware of a 3D PTV system consists of flow markers, an illumination facility, an imaging system, an image digitization and storage unit and a data processing unit. In order to reduce costs it is desirable to use off-the-shelf components as far as possible.

3.1 Flow markers

To visualize a flow for PTV it has to be seeded with small, neutrally buoyant tracer particles. The physical density of the particles should correspond to that of the flow medium and their size should be as small as possible to guarantee good follower behaviour, but large enough to be made visible by suitable illumination. Their shape should be spherical and the surface should be reflecting to maximize the amount of scattered light. In the experi-

ments described here, Pliolite particles (Goodyear Chemical) with mean diameters of either 50 or 200 μm were used. Pliolite particles are not perfectly spherical in shape, but their reflection properties proved to be good.

3.2 Illumination

One of the most important parts of the hardware configuration is the illumination system. To get sufficient signal from small, moving particles in an extended 3D observation volume a light source is necessary which fulfils the following requirements:

- High *intensity* to enable the use of small tracers.
- The light source should be a *point light source*, which makes it easier to shape the light output to a 3D lightsheet collecting the whole output into the desired test volume via an optical system, without iris elements blocking the light.
- To reduce motion effects the light source should be *pulsed* synchronously with the cameras in frequency and in phase.
- The *emission spectrum* should match the sensitivity spectrum of the imaging sensors (with a maximum in the red if solid state sensors are used).
- Homogeneous *intensity distribution* to ensure uniform illumination of the whole observation volume.

Light sources often used in PTV systems are:

- *Lasers*: They offer the advantage of a monochromatic light source and their beam can be shaped into a 3D lightsheet without excessive loss of energy. Disadvantages are the Gaussian intensity profile of the beam and the costs (for example the illumination of a 200 cm^3 volume with 50 μm Pliolite particles requires a 5W Argon Ion Laser).
- *Strobelights*: They operate in very short pulses and are more flexible than lasers. The energy per pulse, however, is often too small.
- *Lamps* with continuous emission: They reduce costs and show often better intensity distributions compared with strobes. The pulsing, however, can only be performed by mechanical shuttering of the beam or electronic shuttering of the cameras; both options lead to a linear loss of light energy.

Fiber optics mouthpieces enable versatile shaping of the beam to achieve an optimal lightsheet with almost rectangular intensity profile.

3.3 Cameras

Only cameras with solid state sensors are suitable if automatic online data processing is envisaged. Tube cameras show larger geometric instabilities and drift behaviour. Film still offers higher resolution but the processing and digitizing of film is usually too time consuming.

Different kinds of solid state sensor cameras can be considered:

- Black and white CCD cameras with consumer electronics video norms (CCIR 25 img/s, NTSC 30 img/s) mean minimum cost, offer high flexibility and are compatible with many display and storage devices. Typical
- sensors have 756×581 pixels (CCIR) or 768×493 pixels (NTSC), respectively. The interlacing of the video signal causes some problems, if moving objects need to be imaged with full spatial resolution, which can be circumvented if an interline transfer type camera is used in combination with an appropriately pulsed light source.
- High resolution cameras offer sensor sizes up to 2048×2048 pixels, but at lower temporal resolution and at much higher cost.
- High Speed cameras offer imaging rates of up to 1000 images per second, but at reduced spatial resolution (e.g. 1000 img/s with 240×192 pixels) and also at high cost.
- Intensified cameras can operate at very low light levels and usually come with standard video norm. Due to the intensifier tube and the fiber connection to the CCD chip the image quality is reduced.

3.4 Camera Lenses

CCD cameras usually have a standard C-mount, which offers a wide variety of lenses with focal lengths of 3.5–1200 mm. Macro and close-up lenses may be interesting for imaging small volumes, but the reduced depth of focus has to be considered.

3.5 Image digitization and storage

A wide range of framegrabbers are available for the A/D conversion of a standard video signal, some of them with interesting additional features like real time low level image pre-processing. High-resolution and high-speed cameras have their own computer interfaces.

As the processing of the PTV image data will not be possible in video real time in most cases, image sequences have to be stored. The high data rates (standard video ca. 11 MByte/s, high resolution or high speed systems up to 46 MByte/s) pose severe problems, especially when three or four cameras are used simultaneously. A storage on standard computer hard disks in real time is generally impossible. The following options can be chosen:

- *Real time disks*: Disk arrays with a special controller distributing the data on many single disks. Data rates and storage capacities are large enough for all imaginable systems, but costs are high.
- *RAM storage* offers data rates, which are comparable with real time disks, but with lower storage capacities.

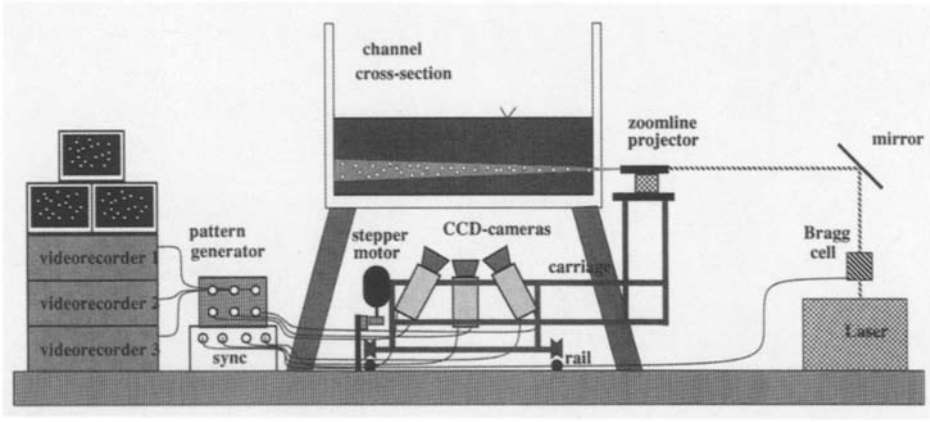

Fig. 2. Hardware installation at laboratory channel

- Analogue *videorecorders* (one per camera) can be used only for standard CCD cameras or intensified cameras. The storage capacity on video tape is very large, the costs are low, but the analogue storage leads to a certain degradation of the image quality. To allow the digitization of synchronous image sequences from more than one videorecorder, a time code has to be supplied to the images before storage.
- Analogue *videodiscs* also offer large storage capacities, but at higher costs for the device and the disks (write once). The larger bandwidth as compared with videorecorders means less image quality degradation. Unlike videorecorders, videodiscs offer random access to images.

3.6 Implementation at ETH Zurich

The configuration of the 3D PTV implemented at ETH Zurich is shown in Fig. 2. The system consists of three or four interline transfer CCD cameras, a 5W Argon ion laser with a zoomline projector for the illumination of an extended 3D testvolume and U-matic videorecorders for analogue image sequence storage. A pattern generator generates a binary pattern as a code for the sequential image number, which is added to the videosignal before storage to allow the recognition of corresponding images on the three or four video tapes. The flow is imaged through a glass section of the channel bottom. Both imaging and illumination system together can be moved with average flow velocity on a carriage parallel to the channel bottom. After recording of a full experiment, image sequences are digitized from all videotapes by a PC equipped with a framegrabber board with RAM storage for only 4 images and a board giving access to the remote control port of the videorecorder. By playing the recorder, continuously grabbing images and evaluating the binary code pattern (which is easily possible from the running video tape in real time), digitizing 4 images, writing them to hard disk, rewinding the tape, playing it again, tracing the image number pattern and digitizing the next 4 images, etc., image sequences of arbitrary length can be digitized completely automatically from all tapes. Data processing is computationally very intensive and should be performed on a powerful computer workstation.

4 Mathematical Model

The fundamental mathematical theorem of photogrammetric 3D coordinate determination is the collinearity condition (Fig. 3, Eq. 1), which states that object point, camera projective centre and image point lie on a straight line.

$$\begin{bmatrix} x_i' - x_h \\ y_i' - y_h \\ -c \end{bmatrix} = \lambda_i \cdot R \cdot \begin{bmatrix} X_i - X_0 \\ Y_i - Y_0 \\ Z_i - Z_0 \end{bmatrix} \tag{1}$$

(X_i, Y_i, Z_i) : object point coordinates
(X_0, Y_0, Z_0) : camera projective centre coordinates
$R = r_{ij}$: elements of 3×3 rotation matrix with angles ω, φ, κ } camera exterior orientation

(x_i', y_i') : image coordinates
(x_h, y_h) : image principle point
c : image principle distance } camera interior orientation parameters
λ_i : scale factor

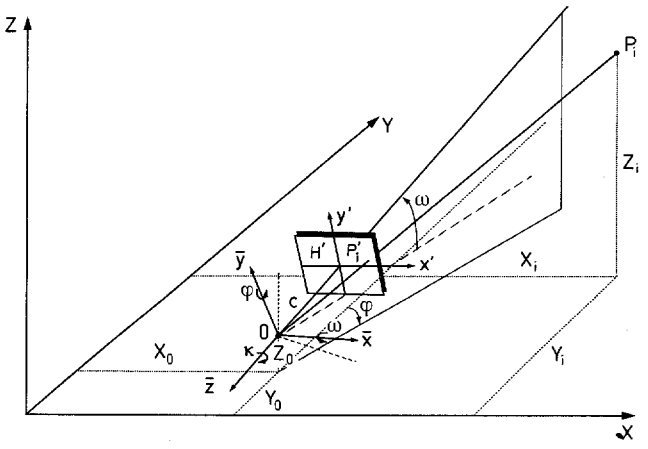

Fig. 3. Collinearity condition (camera model inverted for drawing purposes)

To serve as observation equations in a least squares adjustment for the determination of the unknown parameters (camera orientation X_0, Y_0, Z_0, ω, φ, κ, c, x_h, y_h in the calibration, object coordinates X_i, Y_i, Z_i in the particle positioning), Eq. (1) has to be solved for the image coordinates:

$$x'_i = x_h - c \cdot \frac{r_{11}(X_i - X_0) + r_{21}(Y_i - Y_0) + r_{31}(Z_i - Z_0)}{r_{13}(X_i - X_0) + r_{23}(Y_i - Y_0) + r_{33}(Z_i - Z_0)}$$

$$y'_i = y_h - c \cdot \frac{r_{12}(X_i - X_0) + r_{22}(Y_i - Y_0) + r_{32}(Z_i - Z_0)}{r_{13}(X_i - X_0) + r_{23}(Y_i - Y_0) + r_{33}(Z_i - Z_0)} \quad (2)$$

This mathematical formulation has to be extended to meet the physical realities. One has to consider the fact that each ray from a particle to the sensor passes the three optical media water, glass and air with different refractive indices, which causes a twice broken beam to be handled in the collinearity equation. Furthermore, the image coordinates have to be corrected for effects of lens distortion and effects of the digitization

4.1 Additional parameters for systematic image deformation

The effects caused by lens distortion (e.g. barrel or pillow form distortion) and image digitization are usually compensated by a set of additional parameters, which have to be determined in the calibration together with the parameters of exterior and interior orientation of the cameras. Lens distortion is compensated by a set of 5 additional parameters modelling radial and tangential distortion (Brown, 1971):

$$\bar{x}'_i = x'_i + dx_i \qquad \bar{y}'_i = y'_i + dy_i$$

with
$$dx_i = x'_i \cdot (k_1 r'^2_i + k_2 r'^4_i + k_3 r'^6_i) + p_1 \cdot (r'^2_i + 2x'^2_i) + 2p_2 x'_i y'_i$$
$$dy_i = y'_i \cdot (k_1 r'^2_i + k_2 r'^4_i + k_3 r'^6_i) + 2p_1 x'_i y'_i + p_2 \cdot (r'^2_i + 2y'^2_i) \quad (3)$$

and $r'^2_i = x'^2_i + y'^2_i$ $\quad k_1, k_2, k_3$: radial distortion

p_1, p_2 : tangential distortion

For compensation of effects of image digitization and storage, especially of the often a priori unknown difference between the pixel rate of the CCD cameras and the clock rate of the framegrabber and the global effect of linejitter, an additional affine transformation is performed (El-Hakim, 1986):

$$\tilde{x}'_i = a_0 + a_1 \bar{x}'_i + a_2 \bar{y}'_i \qquad \tilde{y}'_i = b_0 + b_1 \bar{x}'_i + b_2 \bar{y}'_i \quad (4)$$

or – more transparent, but nonlinear – following Albertz and Kreiling (1989):

$$\tilde{x}'_i = x_0 + s_x \bar{x}'_i (\cos\alpha) - s_y \bar{y}'_i (\sin(\alpha + \delta))$$
$$\tilde{y}'_i = y_0 + s_x \bar{x}'_i (\sin\alpha) + s_y \bar{y}'_i (\cos(\alpha + \delta)) \quad (5)$$

$a_0, a_1, a_2, b_0, b_1, b_2$
or $x_0, y_0, s_x, s_y, \alpha, \delta$: parameters of affine transformation.

Due to linear dependencies on the parameters of the collinearity condition only two of the six parameters of the affine transformation can be introduced as unknowns: for instance scale in x'–image coordinate direction and a shear (s_x and δ resp. a_1 and b_2).

All together one receives 16 parameters modelling the geometry of each camera: 6 for exterior orientation, 3 for interior orientation, 5 for lens distortion, 2 for electronic influences. These parameters have to be determined in a system calibration before an experiment is performed.

4.2 Multimedia geometry

The effect of a ray being twice broken due to different refractive indices in the optical path through water, glass and air leads to a multimedia geometry model. Knowing the camera calibration data, the refractive indices and the interfaces between the different optical media, this effect can be strictly modelled.

4.2.1 Development of a multimedia module

If the glass wall separating water and air can be considered a plane parallel plate, a simple module based on Snell's Law can be developed, which can be implemented into the collinearity condition Eq. (2). This module computes a radial shift of each object point relative to the nadir point of the respective camera (Fig. 4), which can be used as a correction term in Eq. (2). If the X–Y plane of the coordinate system is chosen parallel with the plane

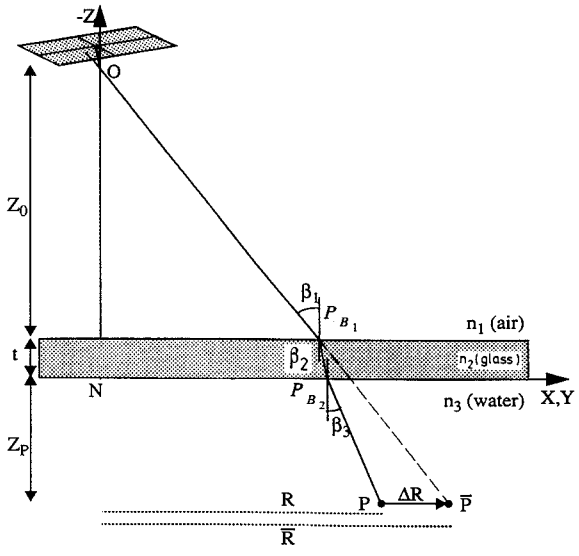

O (X_0, Y_0, Z_0)	:	camera projective center
N (X_0, Y_0, 0)	:	camera nadir point
P (X_i, Y_i, Z_i)	:	object point
$\bar{P}$ ($\bar{X}_i$, $\bar{Y}_i$, Z_i)	:	radially shifted object point
P_B (X_B, Y_B, Z_B)	:	break point
R	:	radius in X/Y-plane
n_1, n_2, n_3	:	refractive indices
β_1, β_2, β_3	:	angles in Snell's Law

Fig. 4. Radial shift for compensation of multimedia geometry

interface glass/water (air/glass resp.), some simplifications are possible. The procedure is shown in Fig. 4: if the point $P(X, Y, Z)$ in object space is shifted to $\bar{P}(\bar{X}, \bar{Y}, Z)$, the collinearity condition can be applied for P using the object coordinates of the shifted point $\bar{P}$. Only a radial shift by $\Delta R(\Delta R > 0$ if $n_2 > n_1$ and $n_3 > n_1)$ parallel to the X–Y plane has to be computed for each point relative to the nadir point of each camera. Thus, rays from different cameras C_j to an object point P are calculated with different points $\bar{P}_j$ with the broken beams still intersecting in P.

$$Z_0 \cdot \tan\beta_1 + t \cdot \tan\beta_2 + Z_p \cdot \tan\beta_3 = R$$
$$\bar{R} = (Z_0 + t + Z_p) \cdot \tan\beta_1 . \tag{6}$$

With Snell's Law

$$n_1 \cdot \sin\beta_1 = n_2 \cdot \sin\beta_2 = n_3 \cdot \sin\beta_3 \tag{7}$$

the system describing the multimedia geometry is complete. Equations (6) and (7) can only be solved iteratively due to the trigonometric functions. If P is chosen as a first approximation for $\bar{P}$ and

$$\bar{R}_{(0)} = \sqrt{(X_p - X_0)^2 + (Y_P - Y_0)^2}, \tag{8}$$

the angle of incidence in the medium n_1 in the first iteration becomes

$$\beta_1 = \text{a tan}\left(\frac{\bar{R}_{(0)}}{Z_0 + t + Z_P}\right). \tag{9}$$

From Snell's Law one gets the angles of incidence and refraction in the other two media:

$$\beta_2 = \text{a sin}\left(\frac{n_1}{n_2} \cdot \sin\beta_1\right), \quad \beta_3 = \text{a sin}\left(\frac{n_1}{n_3} \cdot \sin\beta_1\right) \tag{10}$$

and the correction for $R_{(0)}$:

$$dR = R - (Z_0 \cdot \tan\beta_1 + t \cdot \tan\beta_2 + Z_p \cdot \tan\beta_3). \tag{11}$$

The Eqs. (8)–(11) are used iteratively

$$\bar{R}_{(1)} = \bar{R}_{(0)} + dR \quad \Rightarrow \beta_1, \beta_2, \beta_3 \quad \Rightarrow dR \quad \text{etc.}$$

until $dR < \varepsilon$ (e.g. with $\varepsilon = 0.001$ mm).

Transforming back from polar coordinates to the Cartesian system one obtains the coordinates of the radially shifted point $\bar{P}$

$$\bar{X}_P = X_0 + (X_P - X_0) \cdot \frac{\bar{R}}{R},$$

$$\bar{Y}_P = Y_0 + (Y_P - Y_0) \cdot \frac{\bar{R}}{R}, \quad \bar{Z}_P = Z_p. \tag{12}$$

The nadir point N is defined herein as the orthogonal projection of the camera projective centre O onto the X, Y plane of the chosen local coordinate system. The collinearity condition can then be used with the radially shifted point $\bar{P}(\bar{X}, \bar{Y}, Z)$ instead of $P(X, Y, Z)$.

The convergence of the iterative scheme Eqs. (8)–(11) can be accelerated considerably by introducing an overcompensation factor ($ocf \approx 1.1 \ldots 1.8$) for the calculation of ΔR. The choice of ocf however depends on the refractive indices, the ratio of the light pathlengths in water and air and the angle of incidence itself, so that a constant ocf can only represent an average state. A consequent extension of this idea is the implementation of the radial shift into a reference table (input: depth in water Z_i and radial distance R from nadir point, output: radial displacement factor $\bar{R}/R$). The computational effort needed for the initialization of these reference tables (one for each camera) will be compensated by the reduced processing time for the particle image sequences, even if they are short.

A more general treatment of the multimedia problem has been published by Kotowski (1988). Kotowski allows for an arbitrary number of optical media with different refractive indices separated by plane interfaces, which do not have to be parallel.

4.2.2 Direct solution for the spatial intersection

If short computation times are required and the least squares adjustment consumes too much computation

time, a direct ray tracing and intersection solution can be developed for the spatial intersection following Okamoto and Höhle (1972), under the assumption of plane parallel interfaces as before. This solution however can only be implemented as a spatial intersection and does not represent a functional model suited for a least squares adjustment.

From the image coordinates x', y' of a point corrected for the influence of lens distortion and digitization Eqs. (3) and (4), one can calculate the direction cosine in air

$$\begin{bmatrix} a_1 \\ b_1 \\ c_1 \end{bmatrix} = A \cdot \begin{bmatrix} x'/s' \\ y'/s' \\ -c/s' \end{bmatrix} \quad \text{with } s' = \sqrt{x'^2 + y'^2 + c^2} \tag{13}$$

and determine the intersection of the ray with the air/glass interface (Fig. 4)

$$\begin{bmatrix} X_{B_1} \\ Y_{B_1} \\ Z_{B_1} \end{bmatrix} = \frac{Z_0 - t}{c_1} \cdot \begin{bmatrix} a_1 \\ b_1 \\ c_1 \end{bmatrix} + \begin{bmatrix} X_0 \\ Y_0 \\ Z_0 \end{bmatrix}, \tag{14}$$

where the beam is refracted.
The new direction cosine in glass becomes

$$\begin{bmatrix} a_2 \\ b_2 \\ c_2 \end{bmatrix} = \frac{n_1}{n_2} \cdot \begin{bmatrix} a_1 \\ b_1 \\ c_1 \end{bmatrix} - \left(\frac{n_1}{n_2} \cos i_1 - \sqrt{1 - \left(\frac{n_1}{n_2}\right)^2 + \left(\frac{n_1}{n_2} \cos i_1\right)^2} \right) \cdot \begin{bmatrix} \lambda_1 \\ \mu_1 \\ \nu_1 \end{bmatrix} \tag{15}$$

with $(\lambda_1, \mu_1, \nu_1) = (0, 0, 1)$ in the chosen local coordinate system (plane normal to interface), so that the cosine of the angle incidence i_1 becomes $\cos i_1 = a_1\lambda_1 + b_1\mu_1 + c_1\nu_1 = c_1$.
The intersection of the ray with the glass/water interface is

$$\begin{bmatrix} X_{B_2} \\ Y_{B_2} \\ Z_{B_1} \end{bmatrix} = \frac{d}{c_2} \cdot \begin{bmatrix} a_2 \\ b_2 \\ c_2 \end{bmatrix} + \begin{bmatrix} X_{B_1} \\ Y_{B_1} \\ Z_{B_1} \end{bmatrix}, \tag{16}$$

and the direction cosine in water becomes

$$\begin{bmatrix} a_3 \\ b_3 \\ c_3 \end{bmatrix} = \frac{n_1}{n_2} \cdot \begin{bmatrix} a_2 \\ b_2 \\ c_2 \end{bmatrix} - \left(\frac{n_2}{n_3} \cos i_2 - \sqrt{1 - \left(\frac{n_2}{n_3}\right)^2 + \left(\frac{n_2}{n_3} \cos i_2\right)^2} \right) \cdot \begin{bmatrix} \lambda_2 \\ \mu_2 \\ \nu_2 \end{bmatrix} \tag{17}$$

again with $(\lambda_2, \mu_2, \nu_2) = (0, 0, 1)$ and $\cos i_2 = a_2\lambda_2 + b_2\mu_2 + c_2\nu_2 = c_2$.
Having performed this ray tracing procedure Eqs. (13)–(17) for two corresponding points of two images (the indices l, r denote the left and right image), a spatial intersection can be computed:

$$Z_P = \frac{Y_{B_{2(r)}} - Y_{B_{2(l)}}}{\frac{b_{3(l)}}{c_{3(l)}} - \frac{b_{3(r)}}{c_{3(r)}}}, \tag{18}$$

if the larger component of the baseline between the two cameras is in the Y-coordinate direction, and

$$Z_P = \frac{X_{B_{2(r)}} - X_{B_{2(l)}}}{\frac{a_{3(l)}}{c_{3(l)}} - \frac{a_{3(r)}}{c_{3(r)}}}, \tag{19}$$

if the larger component is in the X-coordinate direction. With the appropriate Z_P, we obtain

$$X_P = \frac{1}{2}\left(X_{B_{2(r)}} + X_{B_{2(l)}} + Z_P \cdot \left(\frac{a_{3(l)}}{c_{3(l)}} + \frac{a_{3(r)}}{c_{3(r)}} \right) \right)$$
$$Y_P = \frac{1}{2}\left(Y_{B_{2(r)}} + Y_{B_{2(l)}} + Z_P \cdot \left(\frac{b_{3(l)}}{c_{3(l)}} + \frac{b_{3(r)}}{c_{3(r)}} \right) \right). \tag{20}$$

This direct solution is considerably faster than the least squares adjustment with the collinearity condition, but it is not a strict solution due to the neglect of the redundant information, and it can only be used (optionally) for the spatial intersection in the particle positioning procedure, but not for the spatial resection in the calibration.

4.2.3 Further influences of the multimedia environment

Besides these exactly modelled effects, the multimedia environment causes some problems which are not contained in the mathematical model but do have a non-negligible influence on the accuracy of results:

- *Aberrations*: The optical system (water–glass–air–camera lens) passed by each ray is not corrected for aberrations if lenses are corrected for use in air. This leads to a degradation of image quality, especially as the cameras are arranged convergently.
- The *dispersion* in water is much larger than in air. The variance of the refractive index in water over the visible spectrum of light is 1.4% in contrast to 0.008% in air (Hoehle, 1971). This leads to colour seams at the edges of imaged objects which will appear as blur in black and white images.
- *Inhomogenities* of the refractive index (due to local pressure and temperature differences) cause deviations from the strict mathematical model, which cannot be modelled.
- Deviations from the *planeness* of the glass walls falsify the angles of incidence.
- The *network geometry* is deteriorated by the smaller intersection angle of rays due to the fact that rays are

broken towards the optically denser medium. This causes larger errors in the Z-coordinates.
- *Diffusion and absorption* in water cause an extinction of light and reduce the image contrast.
- The *diffraction* is not rotationally symmetric with a convergent camera arrangement (Meid, 1991).

All these effects cause a degradation of image quality of multimedia images and systematic errors, which necessarily lead to larger errors in the particle coordinate determination compared with applications in air.

4.3 Handling of the mathematical model

The collinearity condition Eq. (2), in combination with the additional parameters Eqs. (3) and (4) and the multimedia module Eqs. (6)–(12), represents a functional model which is suitable for linearization as observation equations in a least squares adjustment.

$$(x_i', y_i') = f(X_0, Y_0, Z_0, \omega, \varphi, \kappa, c, x_h, y_h, k_1, k_2, k_3, p_1, p_2, s_x, \delta, X_i, Y_i, Z_i). \quad (21)$$

In the calibration procedure this model is being applied for a spatial resection using control points on a calibration frame with known coordinates (X_i, Y_i, Z_i) and introducing the 16 parameters of exterior and interior orientation, lens distortion and affine transformation as unknowns. After the calibration the same model can be used for a spatial intersection, introducing the coordinates of a particle as unknowns. In a photogrammetric bundle solution (e.g. Gruen, 1978), resection and intersection for an arbitrary number of cameras and object points can be solved in one system making the solution more accurate and stable.

The stochastic model for the least squares adjustment of the redundant information contained both in the spatial intersection and the resection is the Gauss–Markov model (e.g. Koch, 1980; Slama, 1980, pp. 77 ff):

$$-e = Ax - l \quad (22)$$

with e: true error
A: design matrix
x: unknown parameters
l: observation vector

which leads to the least squares estimate of the unknown parameters

$$\hat{x} = (A^T P A)^{-1} A^T P l = Q_{xx} A^T P l. \quad (23)$$

Besides the estimates of the unknown parameters, the Gauss–Markov model gives estimates for the accuracy and reliability of the determined parameters and enables the detection of gross errors in the observations.

For the procedure of linearization of the observation equations, inversion of the normal equation system, parameter estimation etc. see (Koch, 1980) or (Slama, 1980, pp. 88 ff).

5 System calibration

To fully exploit the accuracy potential of the method, and to get an estimate of the achievable accuracy, the imaging system has to be thoroughly calibrated. For this purpose a calibration frame (Fig. 5) spanning the entire observation volume is placed into the object space and imaged by all the cameras.

The processing of the calibration images is performed automatically after a user supported preorientation of the cameras. After the calibration, the 16 parameters describing exterior and interior orientation, lens distortion and affine transformation for each camera are known and can be used for the spatial intersections in the particle positioning. The large number of targets on the calibration frame allows half of the points to be used as control points and the rest as checkpoints. If these checkpoints are treated like unknown points (i.e. their coordinates are determined by spatial intersection using the calibration parameters determined from the resection with the other points), the rms deviations between determined coordinates and the given point coordinates are a good estimate of the accuracy of the method.

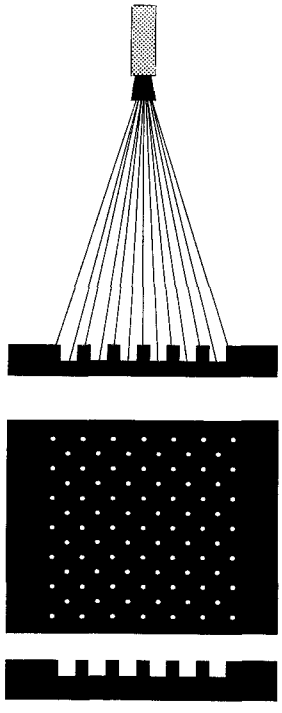

Fig. 5. Calibration frame with 85 known control points separated in two planes

To test the accuracy of the method under ideal conditions a calibration was performed with the calibration frame in air, avoiding the problems of the multimedia environment mentioned in 4.2.3. This experiment yielded the following results:

- The estimated standard deviation of measured image coordinates was $\hat{\sigma}_0 = 0.49$ μm, i.e. about 1/25 of a sensor pixel.
- The RMSE at the introduced checkpoints was 0.013 mm in X, 0.011 mm in Y and 0.024 mm in Z. Divided by a the sidelength of the field of view of about 200 mm, this corresponds to a relative lateral accuracy of about 1:15,000–1:20,000.

A calibration in water with identical equipment and the same field of view yielded significantly less accurate results:

- The standard deviation of measured image coordinates was $\hat{\sigma}_0 = 1.10$ μm.
- The RMSE at the check points was 0.021 mm (X), 0.034 mm (Y), 0.044 mm (Z).

This shows that the accuracy of the hardware system is degraded by about a factor of two as a consequence of the multimedia environment. Moreover, the additional parameters for lens distortion and affine transformation of the calibration in water were significantly different from those determined in air, although the lenses had remained untouched. Furthermore, if the exterior orientation of the calibration in water was combined with the interior orientation and the additional parameters determined in air, the checkpoint differences were increased considerably and showed a strongly systematic pattern. This proves that the influence of aberration etc. (see 4.2.3) is partly compensated by the set of additional parameters. Therefore, it is crucial that the calibration of the system is performed in situ under the optical conditions of the experiment.

The mathematical model also allows the refractive index of water to be introduced as an unknown to be determined together with the other calibration parameters. However, tests (Maas, 1992a) proved that the correlations between the refractive index and other parameters are too high, so that a reliable determination of the refractive index was not possible.

Another problem is the intermediate storage of the image data on analogue videotapes. Some tests to quantify the degradation of the image quality due to the analogue storage showed the following results:

- The noise in the grey values was increased by 50% (from 0.4 to 0.6 grey values).
- Line jitter (Beyer, 1987) was increased by 200% (from 0.04 to 0.12 pixel) due to the smear in the h-sync of the videosignal.
- The RMS of image coordinates of a group of targets measured in each of a sequence of 16 images (i.e. the repeatability of image coordinate measurement in an image sequence) was 0.021/0.010 pixel in the horizontal/vertical image coordinate direction when the image was digitized directly from the camera, and 0.050/0.016 pixel when digitized after intermediate storage on video.
- $\hat{\sigma}_0$ and the rms of the checkpoint differences was increased by about 30%.

This shows clearly that the image quality is significantly degraded by intermediate analogue storage. However, for many users, digital storage facilities are still too expensive to make it a viable alternative.

6 Algorithmic aspects

The chain of automatic data processing from the digitized images to the 3D particle trajectories can be subdivided into the following steps:

- Image pre-processing
- Particle detection, determination of particle image coordinates
- Establishment of stereoscopic correspondences
- 3D coordinate determination
- Tracking in object space

6.1 Image pre-processing

Figure 6 shows an example of a digitized image. Essentially the task of automatic particle identification and particle image coordinate determination in the digital images is trivial, as the particles appear as bright stains on a dark background. After highpass filtering of the images to remove non-uniformities of the background intensity level due to reflections and the nonuniform intensity profile of the light sheet, particle images can be segmented by a simple thresholding algorithm, and image coordinates can be determined with subpixel accuracy by using the grey value weighted centre of gravity of the segmented blobs.

With the large number of particles employed here (typically more than 1000 particles in the illuminated section), however, a problem of particles optically blocking or overlapping each other in one or more views occurs (Fig. 7).

The problem of overlapping particles has rarely been treated in the PTV literature dealing with automatic systems. However, it can be shown (Maas, 1992b), that in a 512×512 pixel image with 2000 particles each covering 10 pixel on average, almost 300 cases of overlapping particles can be expected. The number grows linearly with particle image size and with the square of the number of particles per image. This shows clearly that the problem

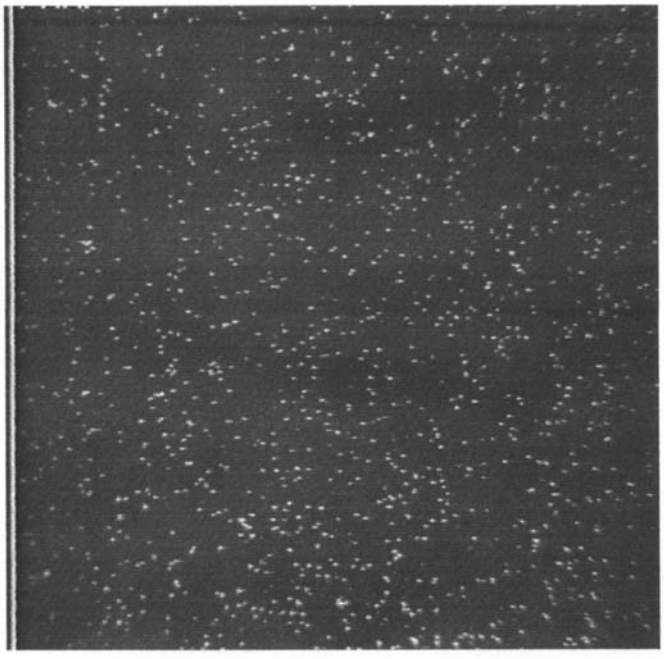

Fig. 6. Digitized image (512 × 512 pixel)

has to be accounted for if the spatial resolution of the system is to be optimized without loss of reliability. Several methods of digital image analysis have been tested to detect and split overlapping images of two or more particles.

- Filtering the images with differential operators proved to be inadequate as they do well in detecting particle image borders, but may fail at pixels where particles touch each other, if the contrast is low.
- Template matching (Gruen and Baltsavias, 1988), morphological operators (Ogniewicz and Kübler, 1989) and Hough transform (Hough, 1962) failed due to the small target size of only 3 × 3 pixels on average.
- Fourier analysis of the particle image borderline (Kuhl and Giardina, 1982) worked well with sharp particle images but failed with slightly defocused images of overlapping particles where the characteristic waist in the borderline is blurred.
- Invariant grey value moments (Teh and Chin, 1988) do not show this sensitivity to defocusing, but higher order moments are rather noise sensitive. For the recognition of overlaps, second order moments proved to be sufficient if only two particles were overlapping, but failed if more than two particles formed a blob.

These problems lead to the development of a modified anisotropic thresholding operator, which searches for discontinuities in the grey values inside segmented blobs and splits blobs if a discontinuity exceeding a certain empirically determined limit is detected. The operator can be characterized by some rules describing a particle image:

- all pixels of a particle image have a greyvalue which is larger than a preset threshold
- a particle image shows exactly one local maximum
- grey values drop continuously inside a particle image
- a pixel representing a local grey value minimum belongs to the particle containing its neighbour pixel with the largest grey value

This operator can be implemented very efficiently and performed satisfactorily. From comparisons with a human supervisor it can be said that in all cases where the human could make a clear decision the operator made the same decision. Most importantly, unlike some of the other methods mentioned above, it does not only indicate cases of overlapping particle images but splits them correctly at local grey value minima.

6.2 Establishment of stereoscopic correspondences

To compute 3D particle coordinates a spatial intersection has to be performed with corresponding image coordinates of a stereopair. The establishment of those stereoscopic correspondences however poses some problems. The particle images do not show any characteristic fea-

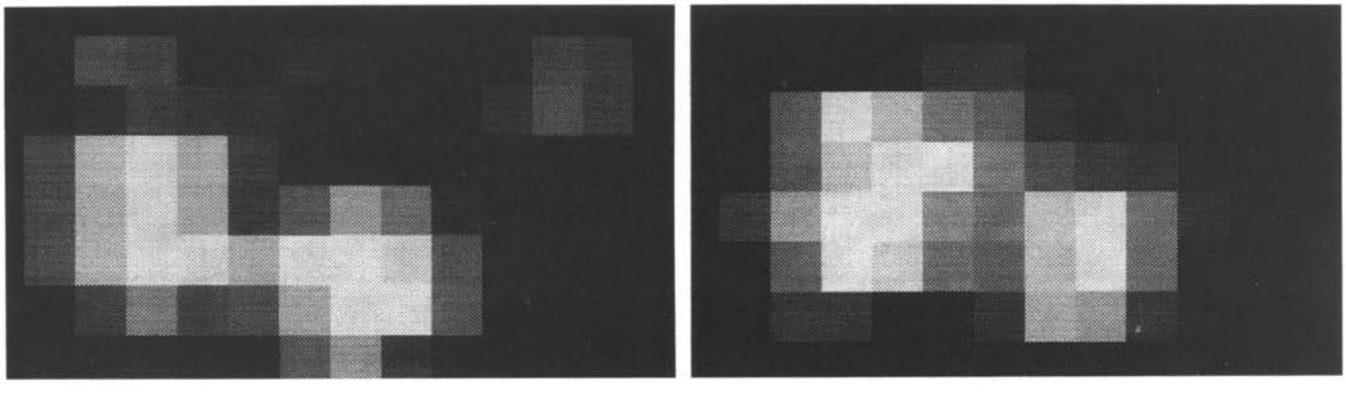

Fig. 7. Examples of overlapping particle images

tures (like colour, size, shape, etc.), which could allow a reliable distinction of particles. The only criterion which can be applied is the geometric constraint of the epipolar line. Knowing the orientation parameters of the cameras from the calibration procedure, proceeding from a point P' in one image an epipolar line in another image can be calculated, on which the corresponding point has to be found. In the strict mathematical formulation this line is a straight line; in the more general case with convergent camera axes, non-negligible lens distortion and multimedia geometry, the epipolar line will be a slightly bent line (Fig. 8), which can be approximated by a polygon. Its length l can be restricted if approximate knowledge about the depth range in object space coordinates is available, which is determined from the knowledge of the illuminated test section (Fig. 9). Adding a certain tolerance width ε to this epipolar line segment (due to data quality), the search area for the corresponding particle image becomes a narrow two-dimensional bandshaped window in image space.

Due to the large number of imaged particles a second problem of ambiguity occurs, as often two or more particle images will be found in the search area. The number of ambiguities grows (Maas, 1992b)

- approximately with the square of the number of particles
- linearly with the length of the epipolar line segment
- linearly with the width of the epipolar search window.

If the particle features do not allow a reliable distinction of particles, these ambiguities cannot be resolved by a system based on two cameras only. With realistic estimates for the number of particles per image and the dimensions of the epipolar search window in a reasonable camera setup, the expected number of ambiguities becomes too large for a two-camera system to yield a robust solution of the correspondence problem (see Table 2).

A consequent solution of the ambiguity problem is the use of a third camera in a setup as shown in Fig. 2 with the camera projective centres forming a triangle (in the ideal case an equilateral triangle) and the camera axes approximately forming a tetrahedron (Fig. 10).

This setup allows the calculation of epipolar line segments intersecting in the image, which can be exploited as shown in the example in Fig. 11:

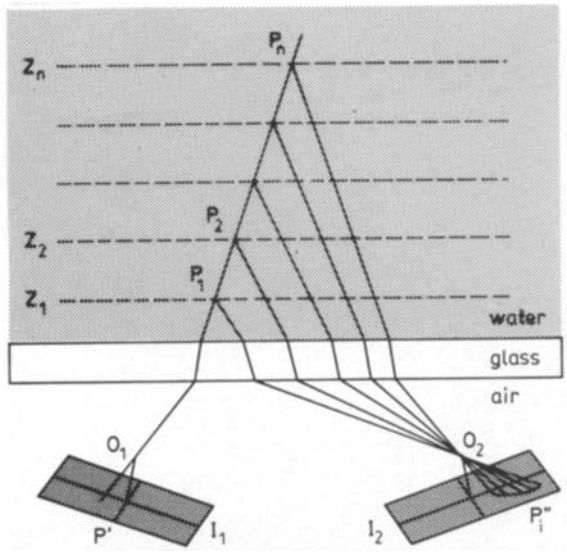

Fig. 8. Derivation of epipolar lines in multimedia geometry

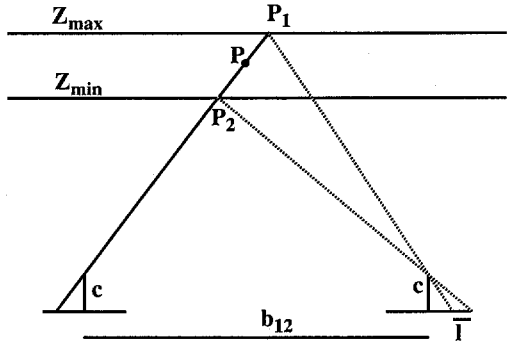

Fig. 9. Length of epipolar search window

Proceeding from a point P' in the image I_1 all epipolar lines $E_{1\to2}$ in I_2 and $E_{1\to3}$ in I_3 are derived, on which respectively candidates P_a'', P_b'', P_c'', and P_d''', P_e''', P_f''' will be found in Fig. 11. An unambiguous determination of the particle image corresponding to P' can neither be found in I_2 nor in I_3. However, if all epipolar lines $E_{(2\to3)_i}$ of all candidates P_i'' in I_2 are intersected by the epipolar line $E_{1\to3}$, there will be a large probability that only one of the intersection points will be close to one of the candidates in

Table 2. Remaining numbers of ambiguities in the establishment of correspondences

	2 cameras	3 cameras collinear	3 cameras in equilateral triangle
$n=1000$, $\varepsilon=10$ µm, $\Delta Z=40$ mm	401	40	35
$n=2000$, $\varepsilon=10$ µm, $\Delta Z=40$ mm	1605	160	140
$n=1000$, $\varepsilon=5$ µm, $\Delta Z=40$ mm	201	10	9
$n=1000$, $\varepsilon=10$ µm, $\Delta Z=80$ mm	802	40	35

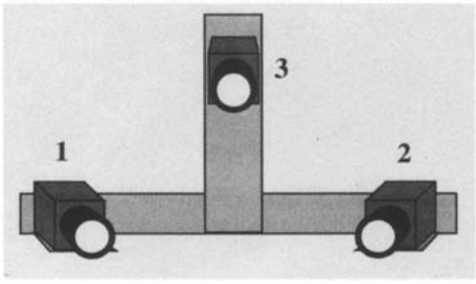

Fig. 10. Arrangement of the three CCD cameras for the method of intersection of epipolar lines

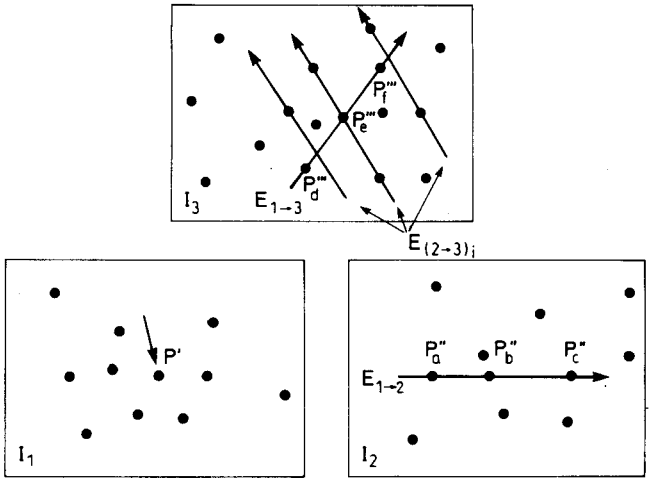

Fig. 11. Principle of intersection of epipolar lines

I_3 (in Fig. 11: P_e'''). This consideration has been implemented via a combinatorics algorithm which tries to find such consistent triplets in the three particle image coordinate datasets and rejects points which are members of more than one consistent triplet. Such an unambiguous consistent triplet is a necessary and sufficient condition for the establishment of correct correspondence. A similar, but iterative approach can be found in Kearney (1991). It can be shown that the method of intersection of epipolar lines can reduce the number of remaining ambiguities by at least one order of magnitude (Maas, 1992b); these remaining ambiguities cause inconsistent triplets and can thus be rejected.

The method described above is the most obvious, but not the only way of exploiting a third camera. Employing a different algorithm, one can also work with three cameras which are arranged such that their projective centres i.e. on a straight line (Maas, 1992b). The expected numbers of remaining ambiguities for the methods discussed above are compiled in Table 2, for realistic assumptions for the number of particles (n), the depth range in object space (ΔZ) and the width of the epipolar search

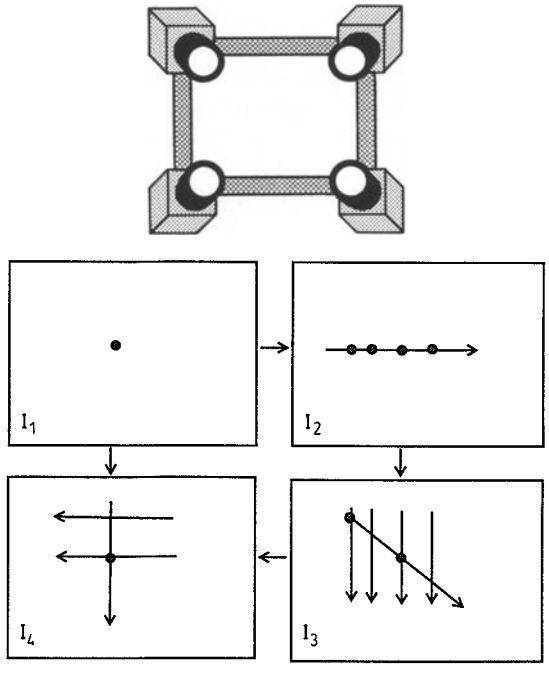

Fig. 12. Example of a four camera arrangement

area (ε) for a base $b_{13}=200$ mm and a camera constant $c=9$ mm:

The number of remaining ambiguities is reduced by at least one order of magnitude for both of the three-camera arrangements compared with a two-camera arrangement. If the number is still considered too large, it can be reduced straightforwardly by the use of a fourth camera with the aim of establishing consistent quadruplets in the four sets of particle image coordinates. The projective centres of a four-camera system can be arranged in a square (Fig. 12), collinearly or in a combination of both.

The principle allows the use of an arbitrary number of cameras, but more than four will rarely be necessary. A four-camera arrangement can be considered ideal: it reduces the number of remaining ambiguities almost to zero, and it even allows a reliable determination of most of those particles which are completely hidden in one of the four images.

6.3 3D coordinate computation

After the establishment of correspondences, the 3D coordinates for the nonambiguous quadruplets (triplets, pairs) can be determined by spatial intersection using either the strict solution via least squares adjustment or bundle solution using Eqs. (1)–(12), or the faster, but less accurate solution Eqs. (13)–(20). Another benefit of the three- and four-camera systems as compared with a two-camera system is improvement of the accuracy of the coordinates of a point by a factor of approximately 1.3 or 1.7, respectively.

The results are datasets with 3D particle coordinates, which are passed to the tracking module to establish correspondences in time (see Malik et al., 1993, Part II of this publication).

7 Results

With our PTV method 3D coordinates of up to 1300 particles could be determined with a three-camera arrangement. The main limitations were the sensor size, the number of overlapping particles and the image quality, which was usually degraded by the fact that none of the light sources mentioned in (3.2) yielded an ideal illumination. The standard deviations of the particle coordinates determined from the least squares adjustment were typically 0.06 mm for the X and Y coordinates and 0.18 mm for the Z coordinate (depth direction perpendicular to camera base) in an observation volume of $200 \times 160 \times 50\ mm^3$. This is worse than the values for checkpoints on the calibration frame, but one has to remember that a moving particle is a much worse target than a well-defined static point. The standard deviations of the particles are influenced by their not perfectly spherical shape for example, but one can expect these effects to be highly correlated in consecutive datasets. To prove the existence of this correlation, a test was performed by recording stationary targets with a similar image quality as far particles from a moving carriage under illumination conditions of the real experiment (Papantoniou and Maas, 1990). The rms variation of 458 determined velocity vectors were 0.028, 0.055, 0.042 mm for the X, Y, Z vector components in a volume of $140 \times 120 \times 10\ mm^3$. This suggests that the correlation between consecutive time steps is relatively high and that the accuracy of the determined velocity vectors is significantly better than the coordinates of a single determined particle. The largest rms error occurs in the moving direction of the carriage, which can be explained by unsteadiness of the carriage velocity due to the stepper motor drive. More importantly, errors in velocity vectors due to coordinate determination do not propagate along trajectories.

The computation times for the 3D coordinate determination on a SUN 4/490 are:

• Highpass filtering	2.0 s/img
• Image segmentation	2.2 s/img
• Establishment of correspondences	5.3 s
• Spatial intersection (see 3.2.2)	1.8 s
• Total	20 s

The initialization of the multimedia reference table (4.2.1) takes 8.3 s, but it has to be performed only once in combination with the calibration.

8 Conclusion

A digital photogrammetric 3D particle tracking velocimetry system is a powerful and versatile flow measurement instrument. To fully exploit the potential of the technique an installation should be based on three or four CCD cameras. Exact mathematical modelling of the multimedia environment and a thorough calibration of the system was found to be crucial for the success of the method. A key point is the careful handling of ambiguities occuring both in the identification of particles and in the establishment of stereoscopic correspondences. With standard CCD cameras up to 1000 simultaneous particles could be tracked with a temporal resolution of 25 velocity fields per second; the lateral accuracy of the determined velocity vectors was about 1:4000 of the camera's field of view, while the depth accuracy was about a factor of 2 worse than the lateral accuracy. High resolution CCDs with up to 4096×4096 pixels or high speed CCDs with up to 1000 images per second (Maas, 1992c) allow variations of the resolution towards higher spatial resolution at the cost of temporal resolution, or vice versa. Recent developments in hardware will considerably influence the design of PTV systems and improve their performance: HDTV (high definition television) will soon make cameras available with sensors of more than one megapixel at temporal resolutions of todays standard cameras. Digital storage facilities will become viable as well if their costs decrease further, and progress in computer workstation performance will make data processing much faster.

Acknowledgements

This work was supported by the Swiss National Foundation for Scientific Research.

References

Adamczyk, A.; Rimai, L. 1988: Reconstruction of a 3-Dimensional Flow Field from Orthogonal Views of Seed Track Video Images. Exp Fluids 6, 380–386

Adrian, R., 1986: Multi-Point Optical Measurements of Simultaneous Vectors in Insteady Flow – a Review. Int. J Heat and Fluid Flow 7, 127–145

Albertz, J.; Kreiling, W. 1989: Photogrammetrisches Taschenbuch. Wichmann Verlag, Karlsruhe

Beyer, H., 1987: Some Aspects on the Geometric Calibration of CCD-Cameras. Proceedings Intercommission Conference on Fast Processing of Photogrammetric Data, Interlaken, Schweiz, 2–4 Juni, S. 68–81

Brown, D., 1971: Close-Range Camera Calibration. Photogrammetric Eng. 37, No. 8

Chang, T.; Watson, A.; Tatterson, G. 1985a: Image Processing of Particle Motions as Applied to Mixing and Turbulence Flow-1. Chem. Eng. Sci. 40, 269–275

Chiu, W.; Rib, L. 1956: The Rate of Dissipation of Energy and the Energy Spectrum in a Low Speed Turbulent Jet. Transactions of the Americal Geophysical Union, Vol. 37/1

El-Hakim, S. F. 1986; Real-Time Image Metrology with CCD Cameras. Photogrammetric Engineering and Remote Sensing, 52, 1757–1766

Gruen, A. 1978: Accuracy, Reliability and Statistics in Close-Range Photogrammetry. International Archives of Photogrammetry, Vol. 22, Part V

Gruen, A.; Baltsavias, E. 1988: Geometrically Constrained Multiphoto Matching. Photogrammetric Engineering 54, 633–641

Hoehle, J. 1971: Zur Theorie und Praxis der Unterwasser-Photogrammetrie. Schriften der DGK, Reihe C, Heft 163

Hough, P. 1962: Method and Means for Recognizing Complex Patterns. U. S. Patent 3069654

Jacobi, O. 1980: Photogrammetric Tracking of a Moving Particle in Running Water. International Archives of Photogrammetry, Vol. XXIII, pp. 369–374

Kasagi, N.; Nishino, K. 1990: Probing Turbulence with Three-Dimensional Particle Tracking Velocimetry. Proceedings International Symposium on Engineering Turbulence – Methods and Measurements, Dubrovnik, September 24–28

Kearney, J. K. 1991: Trinocular Correspondence for Particles and Streaks. Dept. of Computer Science, The University of Iowa, Technical Report 91–01

Koch, K. R. 1980: Parameterschätzung und Hypothesentests in linearen Modellen. Dümmler Verlag, Bonn

Kotowski, R. 1988: Phototriangulation in Multi-Media-Photogrammetry. International Archives of Photogrammetry and Remote Sensing, Vol. XXVII

Koyabashi, T.; Sata, T.; Sekimoto, K. 1989: Velocity Measurement of Three-dimensional Flow around Rotating Parallel Disks by Digital Image Processing. Flow Visualization 1989

Kuhl, F.; Giardina, Ch. 1982: Elliptic Fourier Features of a Closed Contour. Computer Graphics and Image Processing 18, 236–258

Maas, H.-G. 1990: Digital Photogrammetry for Determination of Tracer Particle Coordinates in Turbulent Flow Research. ISPRS Com. V Symposium Zürich, 3.-7.9. 1990, published in SPIE Proceedings Series Vol. 1395, Part I

Maas, H.-G. 1992a: Digitale Photogrammetrie in der dreidimensionalen Strömungsmesstechnik. Ph.D. Thesis No. 9665, ETH Zurich

Maas, H.-G. 1992b: Complexity analysis for the determination of image correspondences in dense spatial target fields. International Archives of Photogrammetry and Remote Sensing, Vol. XXIX

Maas, H.-G. 1992c: High-Speed Solid State Camera Systems for Digital Photogrammetry. International Archives of Photogrammetry and Remote Sensing, Vol. XXIX

Malik, N.; Dracos, T.; Papantoniou, D.; Maas, H.-G. 1993: Particle Tracking Velocimetry in Three-dimensional Turbulent Flows – Part II: Particle Tracking and Lagrangian Trajectories. Exp Fluids, accepted for publication

Meid, A. 1991: Wissensgestützte digitale Bildkoordinatenmessung in aberrationsbehafteten Messbildern. Ph.D. Thesis University of Bonn

Nishino, K.; Kasagi, N. 1989: Turbulence Statistics in a Two-Dimensional Channel Flow Using a Three-Dimensional Particle Tracking Velocimeter. Proceedings on the Seventh Symposium on Turbulent Sheer Flows, Stanford University, August 21–23

Nishino, K.; Kasagi, N.; Hirata, M. 1989: Three-Dimensional Particle Tracking Velocimetry Based on Automated Digital Image Processing. Journal of Fluid Engineering, Vol. III, pp. 384–391

Ogniewicz, R.; Kübler, O. 1989: Lage- und Skalierungsinvariante Skelette zur Robusten Beschreibung und Erkennung binärer Formen. Mustererkennung 1989, Springer Verlag

Okamoto, A.; Höhle, J. 1972: Allgemeines analytisches Orientierungsverfahren in der Zwei- und Mehrmedien-Photogrammetrie und seine Erprobung. Bildmessung und Luftbildwesen 2/1972, 3/1972

Papantoniou, D.; Dracos, T. 1990a: Analyzing 3-D Turbulent Motions in Open Channel Flow by Use of Stereoscopy and Particle Tracking. In: Advances in Turbulence 2, Editors H.-H Hernholz, H. E. Fiedler, Springer Verlag, Heidelberg

Papantoniou, D.; Dracos, T. 1990b: Lagrangian Statistics in Open Channel Flow by 3-D Particle Tracking Velocimetry. In: Eng Turb. Model. Expt. Elsevier

Papantoniou, D.; Maas, H.-G. 1990: Recent Advances in 3-D Particle Tracking Velocimetry. Proceedings 5th International Symposium on the Application of Laser Techniques in Fluid Mechanics, Lisbon, July 9–12

Sata, Y.; Nishino, K.; Kasagi, N. 1989: Whole Field Measurement of Turbulent Flows Using a Three-Dimensional Particle Tracking Velocimeter. 5th International Symposium on Flow Visualization, Prague, August 21–25

Sheu, Y.; Chang, T.; Tatterson, G. 1982: A Three-Dimensional Measurement Technique for Turbulent Flows. Chem. Eng. Commun. 17, 67–83

Slama, C. 1980 (Ed.): Manual of Photogrammetry. American Society of Photogrammetry, Falls Church, Virginia

Teh, Ch.; Chin, R. 1988: On Image Analysis by the Method of Moments. IEEE PAMI, Vol. 10, No. 6, pp. 496–513